Materials Today Energy 28 (2022) 101077

Contents lists available at ScienceDirect

Materials Today Energy

journal homepage: www.journals.elsevier.com/materials-today-energy/

Highly hydrophobic silanized melamine foam for facile and uniform assembly of graphene nanoplatelet towards efficient light-to-thermal energy storage

Amir Reza Akhiani [a], Hendrik Simon Cornelis Metselaar [a, **], Bee Chin Ang [a, b], Mehdi Mehrali [c], Mohammad Mehrali [d, *]

[a] Center of Advanced Materials, Faculty of Engineering, Universiti Malaya, 50603 Kuala Lumpur, Malaysia
[b] Department of Chemical Engineering, Faculty of Engineering, Universiti Malaya, Kuala Lumpur 50603, Malaysia
[c] Department of Mechanical Engineering, Technical University of Denmark, Kgs Lyngby 2800, Denmark
[d] Faculty of Engineering Technology, Department of Thermal and Fluid Engineering (TFE), University of Twente, 7500 AE Enschede, the Netherlands

ARTICLE INFO

Article history:
Received 22 April 2022
Received in revised form
7 June 2022
Accepted 16 June 2022
Available online 27 June 2022

Keywords:
Phase change material
Thermal energy storage
Latent heat
Shape stabilization
Solar energy

ABSTRACT

Solar-thermal technology based on phase change materials (PCMs) has received a lot of attention as a cost-effective and practical way to overcome solar energy intermittency. However, weak photothermal conversion ability and complex preparation processes have hindered the practical application of PCMs. In this work, a new approach for facile, uniform, and firm assembly of graphene nanoplatelet (GNP) through the reaction of graphene oxide (GO) with the silanized melamine foam (MF) is introduced. Here, the deposited amino siloxane layer not only promotes the adhesion and integrity of embedded GNP/GO nanosheets but also facilitates the synthetic route compared to the previous studies. Following the reduction of GO with oleylamine (OA), the hybrid GNP/rGO foams with an integrated network were obtained. The composite PCMs were prepared through the incorporation of paraffin wax (PW) into the hybrid structure. The high hydrophobicity and porosity of the GNP/rGO foams resulted in a high loading of paraffin wax (nearly 97 wt%) and thus large transition enthalpy of 182 J g^{-1}. The GNP/rGO framework provided excellent solar-thermal storage efficiency of up to 92.2%. The PCM composite containing the highest content of GNP (6 wt%) revealed an enhanced thermal conductivity by 87% compared to the unmodified MF/PW composite.

1. Introduction

Solar energy is the most abundant, clean, and renewable energy source that will soon play a crucial role in the global energy transformation [1]. However, solar energy is unreliable as it is naturally intermittent, erratic, and periodic, thus inducing a disparity between supply and demand [2]. A promising avenue to address this looming challenge is using phase change materials (PCMs) to provide an on-demand, reliable, steady, and stable energy supply [3]. Therefore, solar-thermal technology based on PCMs has emerged as a solution to deal with the intermittency of solar energy [4]. To put it simply, PCMs store solar energy in terms of latent heat during sunlight and release the heat when it is demanded [5]. Among the variety of PCMs, organic PCMs are particularly attractive as they are non-toxic, have a high energy density, no supercooling, and stable physical and chemical properties, etc. [6]. However, the low photo-absorption efficiency, poor thermal conductivity, and liquid leakage problem of organic PCMs restrict their widespread practical application [7].

Incorporating nano additives and three-dimensional (3D) network confinement are two practical approaches to obliterate these challenges [6]. Carbon nanotubes (CNTs) [8], graphene nanoplatelets (GNP) [9], reduced graphene oxide (rGO) [10], and boron nitride (BN) [11] are well known nano additives to enhance the PCMs thermal properties. However, a high mass fraction of nano additives is required to form a conductive percolation network and overcome the interfacial thermal resistance between nano additives and PCM. Such a high content of nano additives

* Corresponding author.
** Corresponding author.
E-mail addresses: h.metselaar@um.edu.my (H.S. Cornelis Metselaar), m.mehrali@utwente.nl (M. Mehrali).

https://doi.org/10.1016/j.mtener.2022.101077

compromises the capability of PCMs to store thermal energy due to the presence of inactive mass [12]. Alternatively, 3D incorporated PCMs can present higher thermal conductivity at a relatively low filler content due to the large surface area and thermal conductive pathway provided by the 3D structure [13]. Therefore, porous confinement is the most straightforward approach to improve thermophysical and photo-thermal properties of PCMs.

Recently, the Melamine foam (MF) template strategy has shown great potential for energy storage owing to its low cost, excellent elasticity, lightweight, and porous structure [14]. Along with these thoughts, Xue et al. [15] implemented cellulose nanofiber (CNF) to disperse GNP and wrap the MF skeleton, followed by an ice-templated method and carbonization at 800 °C to construct the 3D structure. In another study, Xue et al. [16] incorporated GO to absorb GNP nanoparticles into MF structure through freeze-drying at −40 °C for 48 h and carbonization at 800 °C for 3 h in a nitrogen atmosphere to obtain rGO/GNP aerogel. Lio et al. [17] reported rGO coated melamine foam through the dip-coating method followed by chemical reduction, freeze-drying, and finally carbonization at 1400 °C. However, since MF exhibits a low surface charge, there is no strong interaction between the nanoparticles and the foam framework. Hence, the implemented electrostatic assembly is inadequate for fabricating an integrated conductive network [18]. Moreover, carbonization at high temperatures to form a conductive path results in the deterioration of the mechanical properties and significant shrinkage of polymer foam. Therefore, proper modification of MF is required to improve the adhesion and integrity of attached nanoparticles and eliminate the complicated and high temperature preparation processes.

In this work, GNP was continually wrapped via self-assembly of GO on the surface of the MF skeleton modified with a hydrophobic amino siloxane layer. The introduced active amino groups substantially enhanced interface interaction between GO and MF substrate to construct the 3D thermally conductive network. GNP is used to enhance photon captor ability and thermal conductivity of the composite; however, it is very difficult to directly incorporate GNP into MF due to the absence of functional groups. Therefore, GO is employed as the intermediary coupling agent because first, its rich surface functional groups can react with the silanized MF, and second, it forms the strong π-π interaction with the embedded GNP nanosheets. These reactions are responsible for the facile, uniform, and firm assembly of GNP on the MF skeleton, which eliminates its tendency to aggregate or detach during the convenient air-drying process. With the resulting GNP/rGO heat-conducting network, the fabricated composites display enhanced thermal conductivity, outstanding latent heat retention, and high solar absorption ability. Therefore, the GNP/rGO composite PCM with these comprehensive properties is deemed to have tremendous potential applications in real-time solar-thermal energy conversion systems.

2. Experimental and characterization methods

2.1. Materials

Melamine foam was obtained from a local department store with a density of around 8.7 kg m^{-3} The graphite flakes were purchased from Sigma-Aldrich (+100 mesh). (3-aminopropyl) trimethoxysilane 95% (APTMS), oleylamine 80–90% (OA), dichloromethane 99.5% (DCM), toluene 99.8%, isopropanol 99.5% (IPA), and ethanol 99.8% were purchased from Fisher Scientific. Paraffin wax with a melting point of around 58 °C was acquired from R&M chemicals. Graphene nanoplatelets (GNP) were supplied by XG Sciences with a lateral dimension of 1–2 μm and an average surface area of 300 m^2 g^{-1}. All the reagents were used as received without further purification.

2.2. Preparation of silanized MF (SMF)

Silanized MF was prepared through a simple solution-immersion method. The MF was punched into a disk shape (diameter of 13 mm and thickness of 3 mm). Round MF was washed with ethanol and distilled water (DW) in a bath-sonicator to remove any impurities and dried at 70 °C for 12 h. Dried MF was immersed in 4 mL toluene containing 100 μL APTMS and placed on an orbital shaker for 3 h to accomplish the silanization reaction at room temperature. To remove the unreacted APTMS, it was washed with toluene and dichloromethane and dried at 120 °C for 4 h. For comparison, amino-siloxane oligomers (ASO) were extracted after drying the residual APTMS solution.

2.3. Preparation of the SMF-GNP/rGO (SMG)

Briefly, a specific amount of GNP was added into a solution of IPA/DW (volume ratio 1:1) and after tip-ultrasonication for 10 min, a homogeneous GNP solution was made. GO slurry (prepared from graphite flakes, following a simplified Hummers' method [10]) was added to the GNP solution while stirring to give a concentration of 1 mg/mL and was treated by bath-sonication for 1 h. A round shape SMF was then soaked in the solution for 1 h for complete infusion of the solution into the pores of the SMF. The SMF- GNP/GO was then put into an OA/IPA (5 μL/mL) solution and reduced in a glass vial at 90 °C for 6 h. After washing with IPA and natural drying, the hydrophobic SMF-GNP/rGO was obtained and abbreviated as SMG*x*, where *x* denotes the concentration (mg/mL) of the GNP in the solution.

2.4. Preparation of the SMF-GNP/rGO-PCM composite (SMGP)

The phase change composites were produced by implementing the vacuum-assisted impregnation method. The SMG*x* foams with high porosity were directly immersed in the molten PW at a temperature of 80 °C for 3 h. Since they were highly hydrophobic, PW immediately penetrated into the foam structure. After impregnation, the obtained composite PCMs were defined as SMG*x*P. For comparison, unmodified MF was also impregnated with PW (MFP) through the same procedure. The schematic illustration of the GNP/rGO foam composites preparation process and their corresponding digital images are illustrated in Fig. 1. The mass content of fillers, together with the composition of the impregnated foams, were calculated from the TGA results and are listed in Table S1.

2.5. Characterization

The structural morphologies were captured using a Hitachi High-Tech SU8030 field emission scanning electron microscope (FESEM) equipped with an energy dispersive X-ray spectrometer (EDX, X-max, Horiba). Fourier transform infrared spectroscopy (FTIR) was performed using a Bruker Tensor 27 in the wavenumber range of 4000 cm^{-1} to 400 cm^{-1} operated in attenuated total reflectance (ATR) mode. X-ray diffraction (XRD) patterns were obtained from PANalytical Empyrean with the 2θ range of 5° to 80° using Cu Kα radiation (λ = 1.54060 Å). Raman spectroscopy was performed using a Renishaw InVia-Reflex confocal microscope equipped with a 633 nm laser. X-ray photoelectron spectroscopy (XPS) was carried out on PHI Quantera II with Al-Kα radiation (hm = 1486.8 eV). Differential scanning calorimetry (DSC) measurements were recorded on Mettler-Toledo DSC1 at a heating/cooling rate of 5 °C min^{-1}, and Thermogravimetric analysis (TGA) was

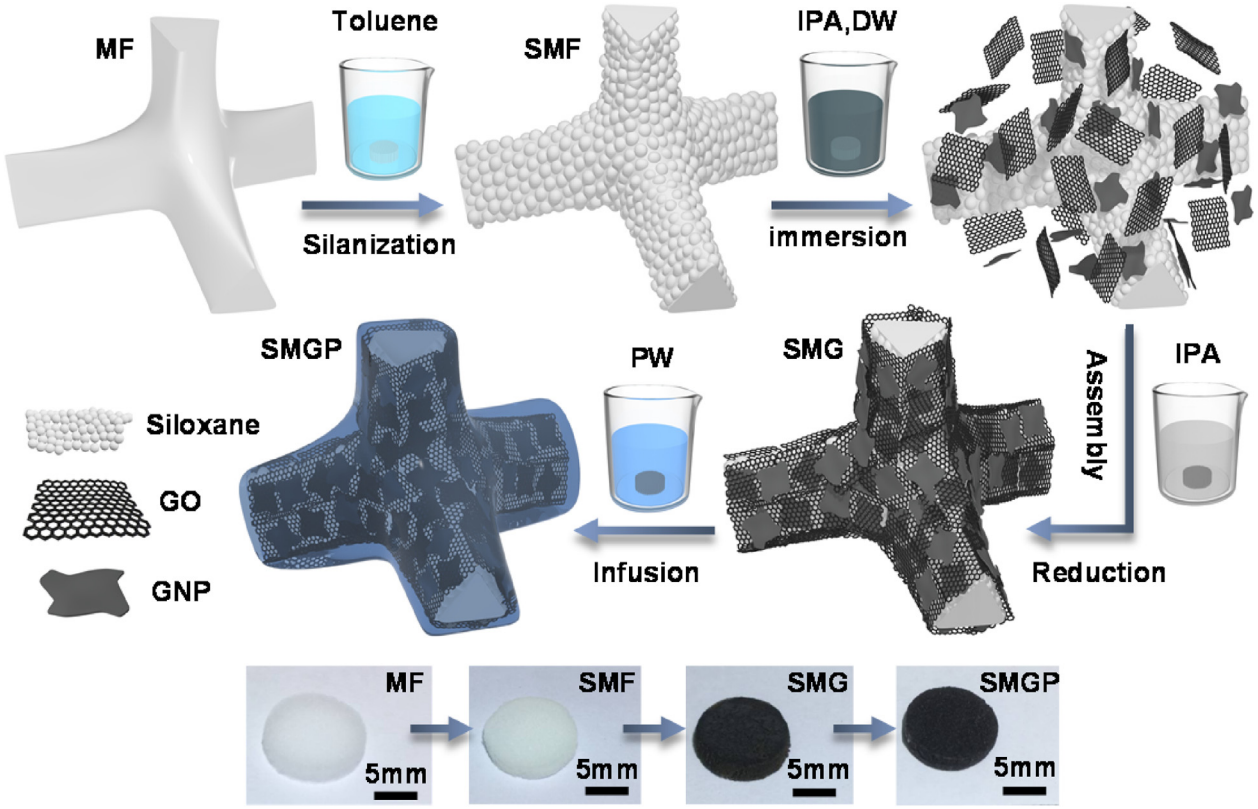

Fig. 1. Schematic illustration of the GNP/rGO foam composites preparation procedure and their corresponding digital photos.

performed using the Setaram Setsys EVO unit equipped with a TGA module from 30 °C to 600 °C under nitrogen purging at a heating rate of 10 °C min^{-1}. Thermomechanical analysis (TMA) was carried out by the Setaram Setsys EVO unit equipped with a TMA module from 30 °C to 120 °C with a heating rate of 5 °C min^{-1} at a constant force of 0.02 N, in the nitrogen atmosphere. Thermal diffusivity measurements were performed by NETZSCH LFA467 at 25 °C. Thermal conductivity (K) was calculated as $K = \alpha \times \rho \times C_p$, where α is the thermal diffusivity, ρ is density, and Cp is the specific heat capacity. The water contact angle was measured using a Data-Physics OCA 15 EC optical contact angle goniometer. The apparent porosity of the porous foams was estimated through the Archimedes method, following the ASTM C1039-85 standard (SI Eq. S1).

The photo-thermal performance of PCM composites was tested under a solar simulator (Newport 67005, 150 W xenon lamp) equipped with an AM 1.5G filter, and a solar power meter (CEM LA-1017) was used to fix the light irradiation power at 1 sun (100 mW cm^{-2}). The sample's temperature was recorded using a data-collecting device (Graphtec, midi logger GL220) using a thermocouple (type-K, OMEGA). The thermal cycling test was conducted in an accelerated thermal cycling system for 1000 cycles from 25 °C to 80 °C [9]. The time of the thermal cycling test was about 10 min for each heating/cooling cycle. Infrared images of the samples were captured using a Seek Compact-pro thermal camera.

3. Results and discussion

Typically, inert imine groups of melamine foam can only interact with nano additive through a weak hydrogen bonding which causes an uneven coating with low adhesion to its surface. To address this issue, active amino groups are introduced onto the foam structure by hydrolytic condensation of APTMS. The detailed mechanism of SMG*x* foams preparation is shown in Fig. 2a. APTMS was first hydrolyzed by a small amount of water in the toluene and attached to the foam structure through hydrogen bonding [19]. Subsequently, condensation of silanol groups formed siloxane polymer, which its further dehydration resulted in the covalent bonding of the amino-silane monolayer onto the foam skeleton [20]. After silanization, GO was covalently attached onto the modified foam surface via ring-opening and condensation reaction of its epoxide and carboxyl functional groups with the introduced amino groups [21]. Simultaneously, GNP nanosheets were evenly embedded in the GO surface through the strong π-π interaction, promoting the formation of the integrated GNP/rGO layer [22]. Finally, OA reduction was applied on the GO surface to restore the sp^2 carbon basal plane, which endows its π-π stacking effect with GNP and improves the hydrophobicity of the interconnected GNP/rGO network [23]. Consequently, the final foam demonstrates the water-contact angle of 139° in Fig. 2b, confirming its beneficial high hydrophobicity to absorb and contain the molten PW properly.

According to the SEM images in Fig. 2c, the MF skeleton shows a highly interconnected cellular structure with a smooth surface and a concave triangle cross-sectional shape. The high porosity of the MF network (99.37%±0.06) makes it a unique substrate for constructing framework-supported nanocomposites. After modification (Fig. 2d), a bulge-like layer formed on the foam surface with an average thickness of around 300 nm (Fig. S1), attributed to the condensation and dehydration of APTMS. It is apparent in Fig. 2e that rGO and GNP nanosheets are uniformly assembled onto the amino siloxane layer and form a densely packed conductive pathway. Interestingly, GNP/rGO agglomerated onto the foam structure and wrapped around instead of segregating out from its surface (Fig. S2) while drying naturally. This effect highlights the key contribution of the amino siloxane layer to the formation of a dense thermal conducting framework. Note that the open-celled porosity of the foam (97.33%±0.13) is totally retained after the

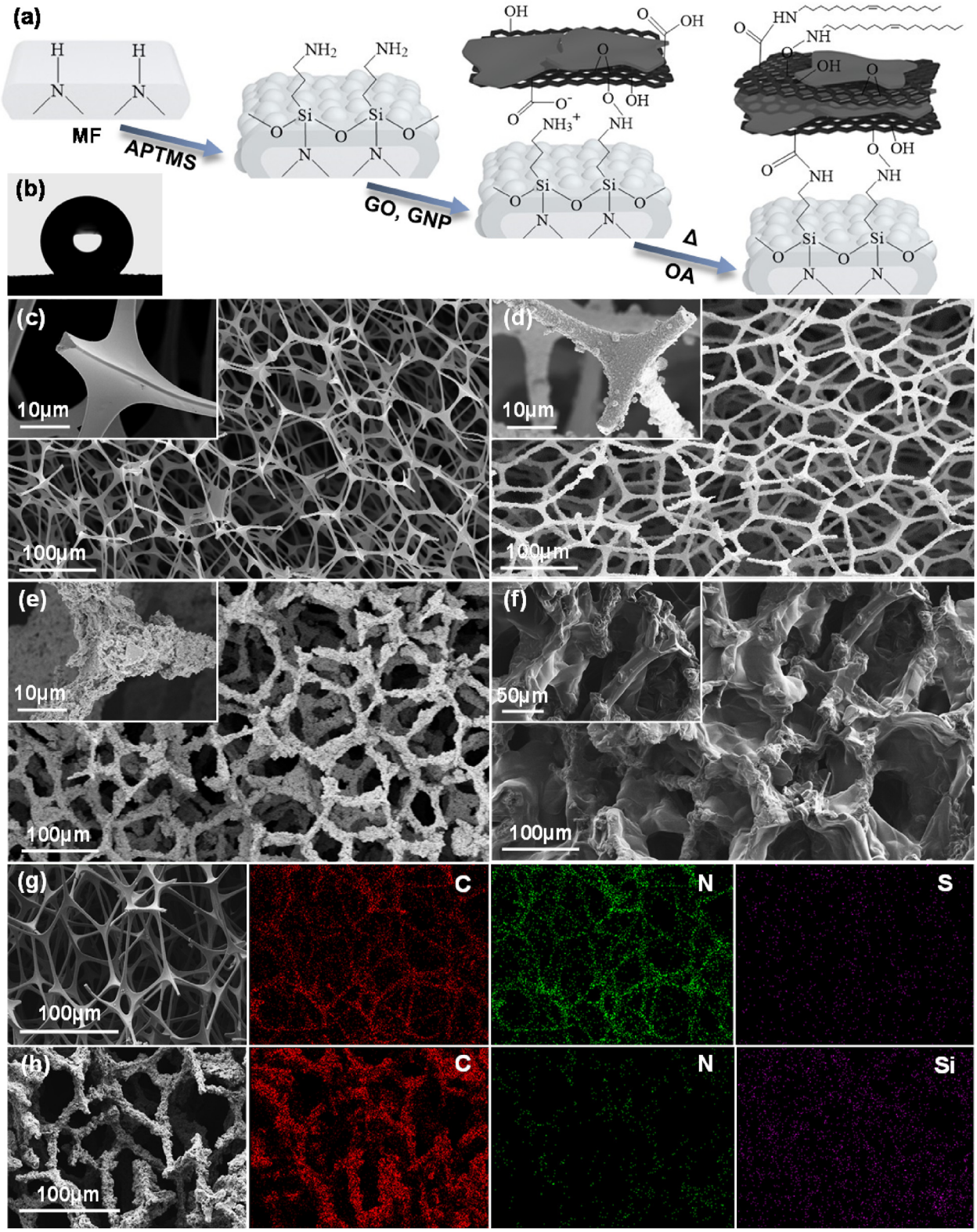

Fig. 2. (a) Schematic illustration of the MF silanization and GNP/rGO assembly. (b) Water contact angle of SMG20. SEM images of (c) MF (d) SMF (e) SMG20, and (f) SMG20P. SEM-EDX elemental mapping images of (g) MF, and (h) SMG20.

GNP/rGO deposition to facilitate efficient PCM penetration. Fig. 2f shows that through impregnation, GNP/rGO foam successfully absorbed PW, and the foam structure was fully covered because of its high hydrophobicity. The high hydrophobicity increases the interfacial interaction between the PW and the foam structure [24]. On the other hand, in Fig. S3 the surface of the MF is still visible, suggesting that the pure MF is not suitable for absorbing PW owing to its hydrophilic nature.

EDX elemental mapping was employed to investigate the elemental distribution in the pristine MF and GNP/rGO foam. C, N, and S elements that were detected in Fig. 2g are consistent with the composition of commercial MF containing the formaldehyde-melamine-sodium bisulfite copolymer [25]. While for the GNP/rGO foam, the C element is predominant, and the locations coincided with the positions of the loaded graphene nanosheets in the corresponding SEM image (Fig. 2h), revealing that the MF matrix was uniformly and fully coated with the GNP/rGO layer.

FTIR and XRD analyses were conducted to verify the formation of the GNP/rGO layer on the foam structure and investigate the chemical structure of the infused PW. As shown in Fig. 3a, only one major peak is observed in the GNP spectrum at 1569 cm^{-1}, related to the C=C stretching vibrations of the sp^2 hybridized carbons on the aromatic rings [22]. However, the GO spectrum reveals several intense peaks, indicating the formation of various oxygen-containing groups during the oxidation process. The broad peaks around 2500 to 3700 cm^{-1} can be assigned to O–H stretching of phenolic and carboxylic groups. The strong peaks at 1718, 1618, 1417, and 1053 cm^{-1} are associated with C=O stretching of the carboxylic group, O–H bending, C=C stretching of the aromatic ring, and C–O stretching of the epoxide group, respectively [26]. For the pristine MF, the absorption peaks at 3337, 1544, 1332, 1159, and 810 cm^{-1} are the stretching vibration of N–H (secondary amine), C=N, C–N, C–O, and bending vibration of the triazine ring, respectively [27]. In the ASO spectrum, the existence of the amino groups can be confirmed by the bands at 690 and 1560 cm^{-1}, belonging to the N–H out-of-plane and the N–H in-plane bending vibrations (primary amine), respectively [28]. Additionally, the Si–O–Si stretching vibration was observed at 1006 cm^{-1}, confirming the formation of long-chain siloxane bonds through hydrolytic polycondensation [29]. The appearance of all characteristic peaks of ASO in the SMF spectrum with the additional triazine ring vibration of MF suggests that the amino siloxane layer was successfully grafted onto the foam. However, the bending vibration of amino moieties almost disappeared in the SMG20 spectra due to their covalent interaction with the GO functional groups. The FTIR spectra of PW and impregnated foams are presented in Fig. 3b. In the spectrum of the pure PW, the peaks at 2916 and 2848 cm^{-1} signify the alkyl C–H stretching of methyl and methylene groups, while the peaks at around 1461 and 719 cm^{-1} represent their C–H bending and rocking vibrations [30]. The spectrum curve of impregnated foams presents the same characteristics peaks as PW, and no new significant peak is detected. This implies that the interactions of PW and the foam components are just physical, and no chemical interactions occurred.

The XRD patterns of the GNP/rGO foam components are presented in Fig. 3c. One sharp diffraction peak appeared for GO at 9.9° and GNP at 26.6°, associated with the (002) crystal plane with an interlayer spacing of 0.89 nm and 0.33 nm based on Bragg's equation, respectively [16]. While, SMF shows broad diffuse scattering, corresponding to the non-crystalline structure of MF and ASO. After the OA treatment, GO and GNP form a hybrid layer, and the characteristic peak of GO disappears in SMG20 as it is conflated with the GNP diffraction peak due to the reduction of the GO sheets. Furthermore, the crystal structures of the PW and impregnated foams were also investigated, as shown in Fig. S4. The diffraction peaks at 21.2° and 23.6° are attributed to the (110) and (200) crystal planes of PW [31]. In contrast, the XRD patterns of the impregnated foams also display the two sharp peaks of PW with no noticeable shift in their positions. This indicates that the crystal structure of PW was not changed, and no new phase was formed during the impregnation process.

Raman spectroscopy was conducted to analyze the microstructure of GNP, GO, and foam components (Fig. 3d). Raman spectra of GNP and GO show typical D and G bands of graphitic

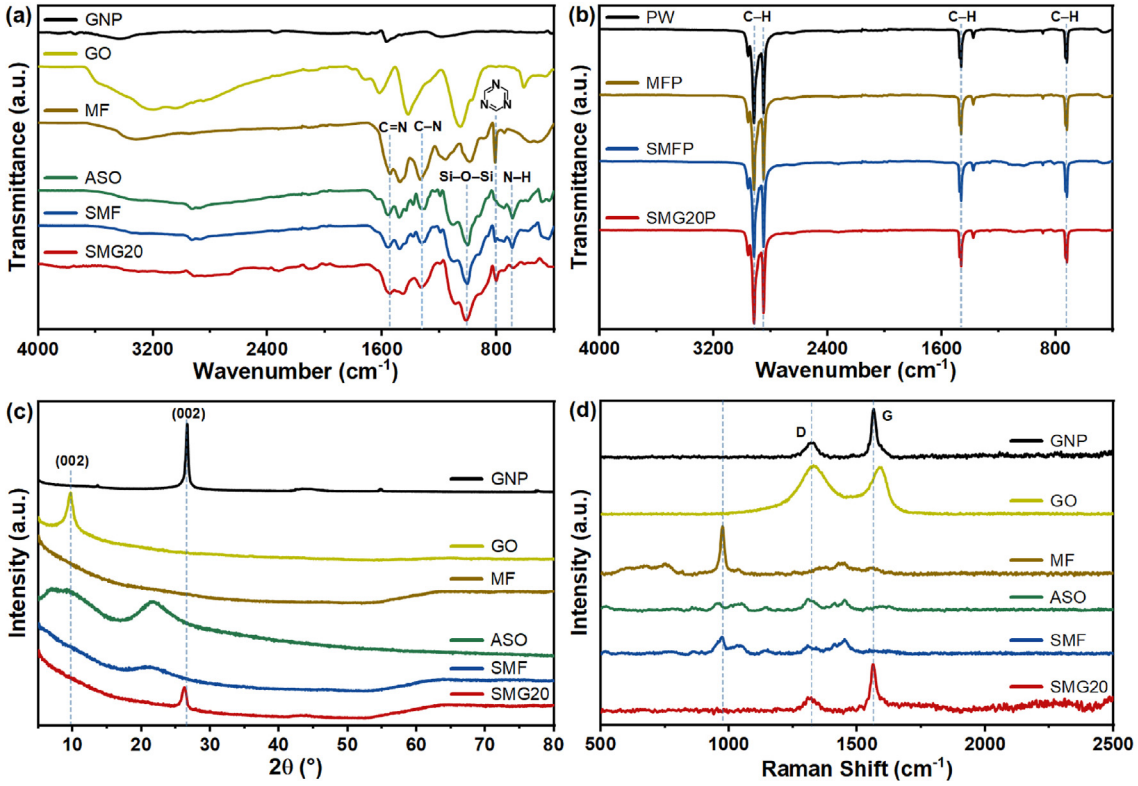

Fig. 3. FTIR spectra of (a) GNP/rGO foam components, and (b) impregnated foams. (a) XRD, and (b) Raman spectra of GNP/rGO foam components.

structures at ~1325 cm^{-1} and ~1575 cm^{-1}, respectively. The D band is related to the vibration of disordered carbon atoms caused by the structural defects, while the G band is linked to the first-order scattering of the E_{2g} vibration of the crystallized graphitic sp^2 carbon network. Therefore, the intensity ratio of the D band and G band (I_D/I_G) is usually used to determine the degree of defects in the graphitic structure [32]. The I_D/I_G of GO (1.06) is significantly higher than GNP (0.32), indicating the electronic delocalization in sp^2 graphene structure due to the existence of oxygen containing functional groups. In the MF spectrum, the most intense peak at 975 cm^{-1} corresponds to the bending vibration of the triazine ring [33]. This peak can be observed in the SMF spectrum, showing the coexistence of the siloxane layer and MF. The Raman spectrum of SMG20 is similar to GNP with the I_D/I_G of 0.33, revealing that the GNP completely covered the foam structure.

XPS was employed further to investigate the silanization and formation of the GNP/rGO layer. In the XPS spectrum (Fig. 4a), low oxygen content (4.21 at.%) was observed for the GNP, while GO shows a high content of oxygen moieties (38.32 at.%) obtained during the oxidation process. The observed elements in the survey spectrum of MF are consistent with elemental mapping results. After silanization, additional silicon peaks appeared, and the oxygen concentration in SMF significantly increased from 13.43 at.% in MF to 21.91 at.%, indicating the presence of the amino silane layer. Moreover, the carbon content is 13 at.% higher in the SMG20 survey spectrum than in the SMF after forming the GNP/rGO layer (Table S2). The high-resolution C1s spectra of the MF is deconvoluted into four peaks assigned to C–C (284.8 eV) of graphitic carbon, C–O (285.9 eV) of ether groups, C=N–C (287.4 eV) of triazine ring, and O–C=O (288.6 eV) of carboxyl groups, respectively (Fig. S5a) [34,35]. However, SMF spectra could be fitted with an additional peak centered at 284.0 (Fig. S5c) corresponding to C–Si component owing to APTMS deposition, which is consistent with the C1s spectra of ASO in Fig. S5b [36,37]. The C1s envelope of the SMG20 sample (Fig. 4b) shows all the components from SMF but with higher intensity of the C–C bond and an extra $\pi-\pi^*$ shake-up satellite peak, resulting from the π-π stacking interaction between the layers of graphene nanosheets [38]. As shown in Fig. S6a, the N1s peak of the MF is fitted with two peaks at 398.7 and 400.1 eV, which are assigned to the triazine ring (=N–) and secondary amine group (–NH–), respectively [39,40]. In addition, the two peaks in the N1s spectrum of ASO (Fig. S6b) at 399.0 and 400.5 eV are attributed to the primary amine ($-NH_2$) and protonated amine group ($-NH_3^+$) [41,42]. A new peak appeared after silanization with a binding energy value centered at 397.9 eV (Fig. S6c) that could be associated with the N–Si component due to the covalent interaction of siloxane with the secondary amine group of MF [43]. In the SMG20 spectra (Fig. S6d), however, the amine peak shifted to a higher energy level caused by the interaction of OA amino groups with the GO functional groups. The High-resolution Si2p XPS spectrum of ASO revealed two types of Si atoms assigned to Si–C (101.8 eV) and siloxane group (102.9 eV), respectively (Fig. S7a) [44]. While as observed in Figs. S7b and c, the new peak at 102.3 eV would be due to the reaction of siloxane oligomers with MF and the formation of the Si–N bond during the dehydration reaction [19]. These findings are consistent with the FTIR and Raman results, which further confirm the formation of the amino siloxane layer, followed by the successful deposition of the GNP/rGO layer on the MF skeleton.

TGA and derivative thermogravimetry (DTG) was carried out to understand the effect of each component on the thermal degradation of the modified foams (Figs. S8a and b). Based on TGA and DTG curves, MF underwent a severe weight loss from 380 °C to 400 °C and further moderate weight loss until 600 °C attributed to the

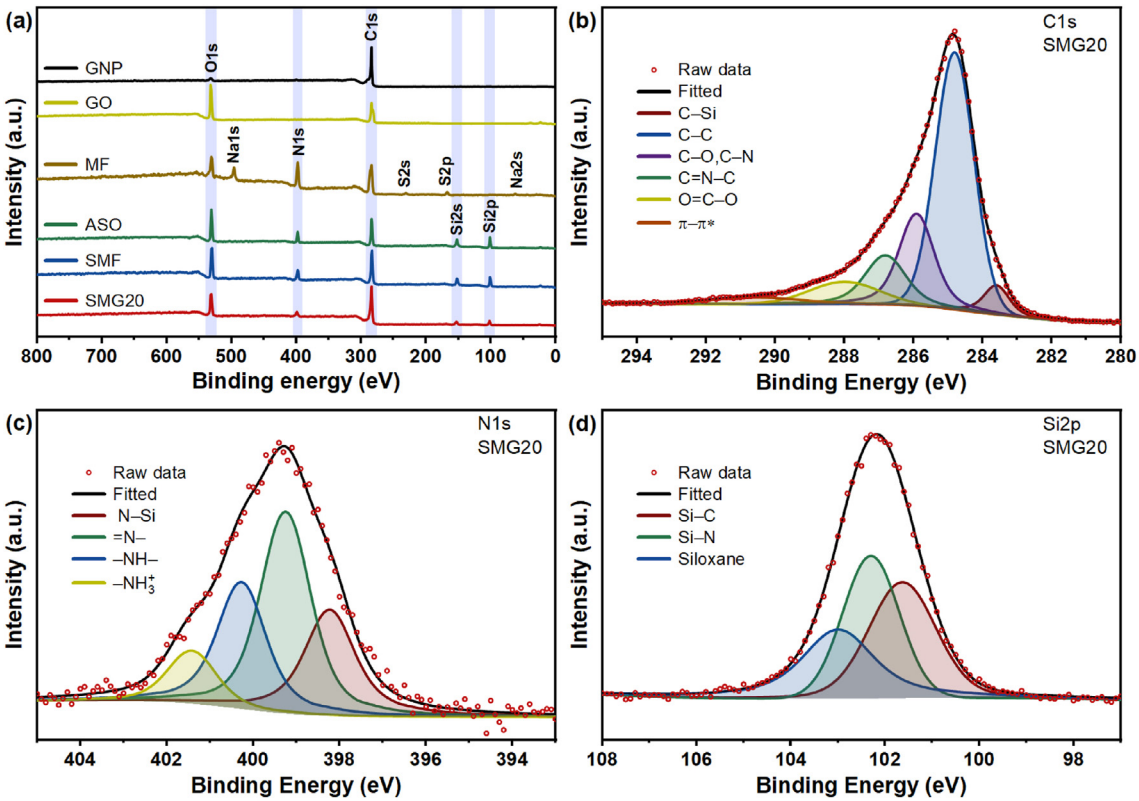

Fig. 4. (a) The survey curves of GNP/rGO foam components, High-resolution XPS spectra of SMG20 (b) C1s (c) N1s, and (d) Si2p.

elimination of methylene linkages and degradation of triazine ring, respectively [45]. For ASO, the first weight loss from 70 °C to 200 °C is due to the physisorbed water and unreacted hydroxyl group. The second mass loss from 390 °C to 520 °C belongs to eliminating its aminopropyl group [46]. Basically, the decomposition of SMF reflects both MF and ASO degradation behavior. But the weight loss of MF in the temperature interval of 380 °C to 410 °C was smaller as the siloxane layer might avoid the rapid decomposition of the triazine ring. After the GNP/rGO incorporation, the total weight loss at 600 °C is only 23% for SMG20 and considering the total weight reduction of SMF (48%), the mass content of GNP/rGO in the hybrid foam structure is calculated to be around 75%. The thermal stability of the PW composites was also investigated, and the corresponding curves are presented in Fig. 5a. The one-step decomposition of the pure PW begins at around 250 °C and completes at about 390 °C. However, the weight loss of the PW composites ends at a higher temperature by increasing the GNP ratio. This phenomenon may be ascribed to the existence of an inflammable GNP/rGO matrix with the large GNP sheets acting as a shield, thus causing a lower degradation rate and a broader mass reduction region. Moreover, the weight proportion of the filler in SMG5P, SMG10P, SMG15P, and SMG20P is estimated to be 1.5, 3.7,6.2, and 8.4% based on their residual ratio at 600 °C. According to these results, PW composites demonstrate good thermal stability at relatively low filler content, which is significant to retain the latent heat capacity of the composites.

Besides thermal stability, mechanical stability is another essential attribute for PCM composites to preserve good performance in practical applications. Hence, TMA analysis was conducted to compare the shape stability of the pure PW with the prepared composites (Fig. 5b). The neat PW showed a slight deformation in the temperature interval of 58 °C to 85 °C and rapid dimensional change after 85 °C due to the solid-solid and solid-liquid phase transition, respectively. On the contrary, all PW composites maintain their shapes even at 120 °C, and only small dimensional changes can be observed. Interestingly, by incorporating more GNPs into the structure, the shape retention of the composites also increased, which can be ascribed to the stiffening and reinforcing effect of GNP sheets on the supporting structure.

The phase change enthalpy is an important parameter for determining the heat energy storage capacity of the PCMs. Thus, the melting and solidifying behavior of pure PW and impregnated foams were evaluated by DSC, and corresponding curves are shown in Fig. 5c and d. The phase change parameters, including melting point (T_m), melting enthalpy (ΔH_m), solidifying point (T_s), and solidifying enthalpy (ΔH_s), are listed in Table 1. Two main peaks are detected during the heating and cooling process of pure PW, which originates from its solid-solid and solid-liquid/liquid-solid transition [47]. The peak patterns of the impregnated foams are almost identical to the neat PW, suggesting the crystallization ability of the PW was not affected by infusion into the GNP/rGO foam. However, in both heating and cooling thermograms, the temperature range of phase transition becomes wider, and the peak width of melting (PW_m) is enlarged. This can be explained by the confinement of the PW in the GNP/rGO network, which hinders its free molecular movement and diffusion of PW while it is melting [15]. Besides, as GNP nanosheet content increased, PW_m of composites became narrower, considering the faster heat transfer of the substrate to melt the infused PW. On the other hand, the ΔH_m and ΔH_s of the composites decreased gradually since a portion of the working substance (PW) was substituted by the GNP/rGO foam. The thermal storage capacity of the impregnated foams was assessed through the enthalpy efficiency (φ) in Eq. (1) and the normalized enthalpy efficiency (η) in Eq. (2) [48].

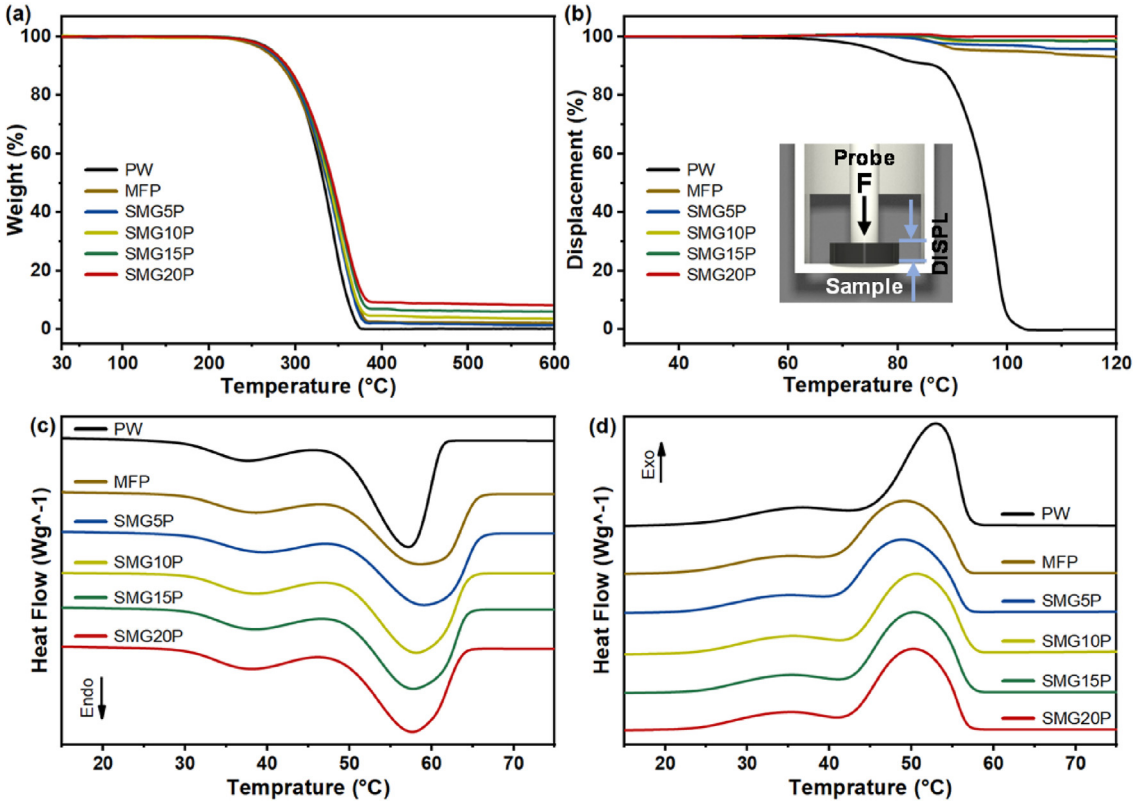

Fig. 5. (a) TGA, (b) TMA, DSC (c) heating, and (d) cooling curves of PW and impregnated foams.

Table 1
Thermal Characteristics of PW and impregnated foams, acquired from the DSC measurements.

Samples	T_m (°C)	ΔH_m (J g^{-1})	T_s (°C)	ΔH_s (J g^{-1})	PW_m	φ (%)	η (%)
PW	56.8	187.1	53.7	189.1	7.2	100.0	100.0
MFP	58.1	182.2	49.5	183.9	11.1	97.3	99.3
SMG5P	58.6	184.8	49.3	185.4	10.7	98.4	99.9
SMG10P	57.9	183.7	51.0	184.7	9.9	97.9	101.7
SMG15P	57.3	182.9	50.8	183.6	9.7	97.4	103.9
SMG20P	57.3	181.2	50.6	182.2	9.3	96.6	105.5

$$\varphi = \frac{\Delta H_{m,foam} + \Delta H_{s,foam}}{\Delta H_{m,PW} + \Delta H_{s,PW}} \times 100 \quad (1)$$

$$\eta = \frac{\Delta H_{m,foam} + \Delta H_{s,foam}}{\omega(\Delta H_{m,PW} + \Delta H_{s,PW})} \times 100 \quad (2)$$

where $\Delta H_{m,foam}$, $\Delta H_{s,foam}$, $\Delta H_{m,PW}$ and $\Delta H_{s,PW}$ denote the melting enthalpy and solidifying enthalpy of the impregnated foams and neat PW, respectively, while ω denotes the weight percentage of the PW in the composites obtained from the TGA results. Obviously, the filler loading was extremely low, and even at the highest GNP content, SMG20P has maintained a high enthalpy efficiency of 96.6%. Impressively, the η of the composites is more than 100%, meaning that the crystallinity of PW was improved after impregnation. This can be caused by the hydrophobic interaction between PW and GNP/rGO foam, which could serve as a better heterogeneous nucleating agent while increasing the GNP content [49].

The shape stability of the PW and impregnated foams is also visually tested by placing the samples directly on the heating stage and increasing the temperature to 100 °C. The state of the PW and impregnated foams during the heating process was captured using the digital camera, as presented in Fig. S9 and Video S1. All the samples are solid at ambient temperature with an initial round-like shape (Fig. S9a). Once heated to 100 °C, pure PW began to melt with visible leakage at the bottom until it completely melted into a liquid (Fig. S9b). In contrast, the impregnated foams remain intact, MFP and SMG5P exhibit a small amount of leakage, but no leakage exists for the rest of the PCM composites. Actually, the infused PW in the foams was also melted, but due to the strong hydrophobic interaction, molten PW was well confined in the foam network. These results evidently reveal that the GNP/rGO foam is relatively efficient in shape-stabilizing and suppressing the leakage of the composite.

The prominent photon captor attribute and high thermal conductivity of GNP sheets make the hybrid GNP/rGO structure an ideal light-to-thermal conversion substrate for solar energy harvesting applications [50]. Hence, a photothermal conversion testing device was designed (Fig. 6a) to comparatively evaluate the photothermal conversion performance of the impregnated foams. Fig. 6b presents the temperature evolution of the MFP and the GNP/rGO foam composites with time in the presence and absence of light irradiation. Under radiation, the temperature of pure PW rises slowly and reaches its maximum temperature of only about 49 °C because of the poor solar absorbance of its white surface. On the contrary, GNP sheets on the surface of the hybrid GNP/rGO foams functioned as the medium to absorb solar energy and transform it into heat. Subsequently, generated heat was delivered to the PCM through the heat conduction channels in the GNP/rGO foam structure. Thus, the temperature of the composites rises rapidly until reaches the inflection point, indicating the complete phase

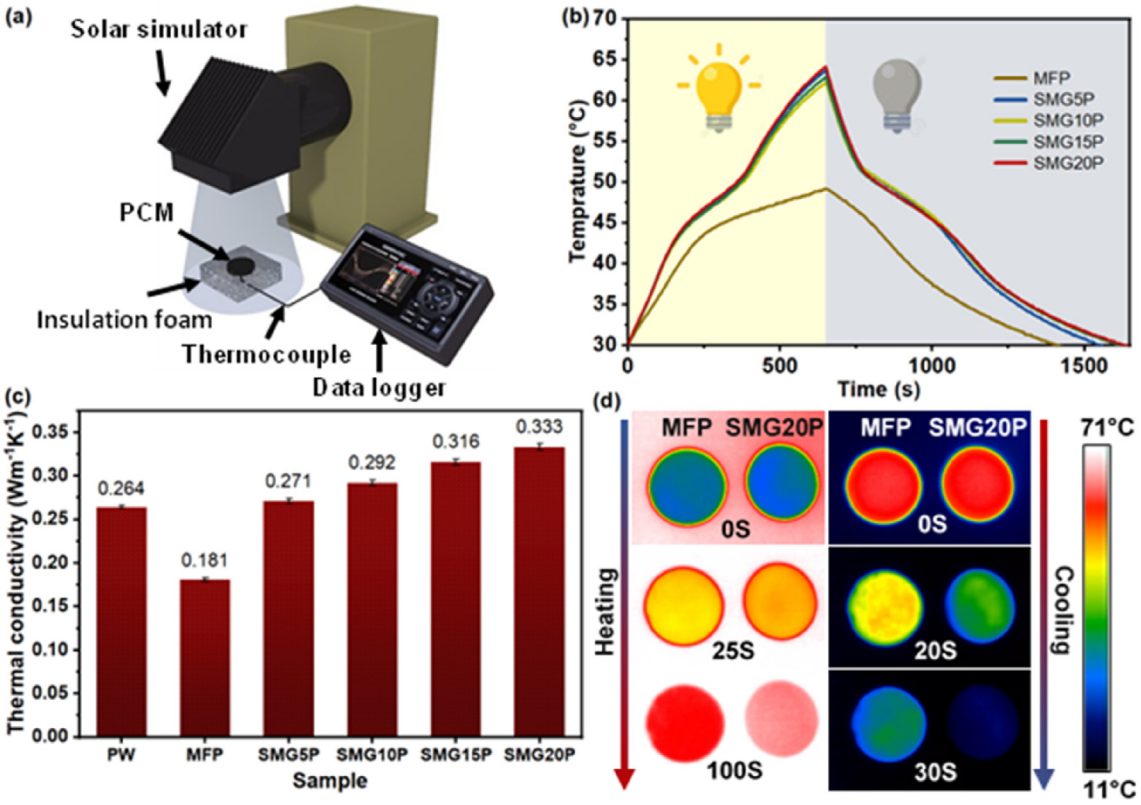

Fig. 6. (a) Schematic illustration of light-to-thermal energy conversion device. (b) Temperature evolution curves of impregnated foams under the simulated sunlight irradiation. (c) Thermal conductivity of PW and impregnated foams. (d) Thermal transport evolution of MFP and SMG20P during heating and cooling process.

Table 2
Comparison of enthalpy efficiency (φ) and photothermal storage efficiency (η) between the SMG20P composite and the related composite PCMs reported in the literature.

Nanofiller	Foam preparation		PCM	φ_f (%)	φ (%)	η (%)	Reference
	Method	Temperature °C					
GNP/GO	Mixing, freeze drying	90	PEG	4.3	99.3	84.4	[52]
Graphene	Baking, CVD	1000	PW	4.8	95.7	89	[53]
rGO	Mixing, freeze drying	90	PW	2.2	98.8	79.9	[54]
rGO	Supercritical drying, annealing	600	PW	6.0	98.2	77	[55]
GNP/rGO	Freeze drying, CVD	1000	PW	14.0	87.1	90	[56]
GNP	Freeze drying, annealing	800	PW	4.1	98.4	78	[15]
GNP	Freeze drying, annealing	1500	PEG	20.8	81.9	40.7	[57]
TiO_2/rGO	Hydrothermal, freeze drying	120	PW	7.6	80.7	89.9	[58]
GNP/rGO	Immersion, airdrying	90	PW	8.4	96.6	92.2	This work

transition of the infused PW. By the end of the irradiation, the foam composites with more GNP content reached slightly higher temperatures owing to their enhanced photothermal efficiency. When the light was switched off, composites began to cool quickly until the appearance of another plateau while PW solidifies and releases the stored thermal energy. To investigate the photothermal conversion ability of the prepared composites, the following equation is employed to determine their solar-thermal storage efficiencies (η) [51]:

$$\eta = \frac{m\,\Delta H}{I\,A\,\Delta t} \tag{3}$$

where m and ΔH signify the total mass of the samples and their melting enthalpy obtained from the DSC, respectively; I, A, and Δt represent the light source irradiation intensity, the sample surface area, and the melting interval, respectively. Thus, the calculated η of the SMG5P, SMG10P, SMG15P, and SMG20P is 84.2%, 88.0%, 90.9%, and 92.2%, respectively. Considering the similar weight, size, and melting enthalpy of the samples, the reason for increasing the photothermal storage efficiency of the composites is the shorter phase change period induced by the elevation of the heating rate as GNP content increases. The excellent solar-thermal storage efficiency of the GNP/rGO foam composites would offer promising choices for utilization in actual solar energy storage applications.

The variation of the thermal conductivity of the PW and impregnated foams is shown in Fig. 6c. Compared with the pure PW, the thermal conductivity of the MFP is reduced by 30%, while the GNP/rGO foams exhibit an enhanced thermal conductivity of up to 32%, which is significant considering the minimal amount of the incorporated filler. The lower thermal conductivity of the MFP can be ascribed to its low density, given that the hydrophilic MF could not contain the PW properly. Conversely, the highly hydrophobic attribute of the GNP/rGO foams causes the strong interfacial interaction with PW leading to a proper infusion of PW into the porous structure. Furthermore, the conductivity enhancement of SMG20P was 87% higher than the MFP due to the formation of the GNP/rGO heat-conducting layer and the construction of the continuous network structure. For the SMG5P and SMG10P, the slight enhancement of k is mainly attributed to the small recovery degree of the conjugated structure of graphene sheets, owing to the partial reduction of rGO by OA. However, by increasing the filler content, the inherent high thermal conductivity of GNP sheets lowers the interfacial thermal resistance among rGO sheets and accelerates thermal transport.

The thermal conduction capacity of the MFP was also visually compared with SMG20P by evaluating their temperature response while subjected to heating and cooling. An infrared thermal camera was used to record the surface temperature evolution when the composites were placed on the hot and cold platform, as presented in Fig. 6d and Video S2. During the heating process, the temperature rise in SMG20P was faster than that in MFP until the melting of the confined PW occurred, and consequently, a constant temperature plateau appeared. After completion of the melting transition, the temperature began to increase more rapidly for the SMG20P because of the incorporated conductive structure. As expected, similar results could also be observed during the cooling process, and SMG20P exhibited a better heat transfer rate. Furthermore, the uniform color of the SMG20P surface confirms a more homogeneous heat distribution, which can be attributed to the dense and uniform infusion of PW into the foam. The higher heating and cooling rates of SMG20P indicate that it has faster heat transport properties, thus possessing promising thermal preservation capability.

The prolonged thermal durability of the SMG20P was evaluated by comparing the DSC and FTIR results of the sample before and after undergoing 1000 heating/cooling cycles. As demonstrated in Fig. S10a, the DSC curves before and after the cycling test almost overlap with each other, signifying the minimal change in the phase change properties of the SMG20P. Besides, no clear changes in the peak position and peak intensities are observed from the FTIR spectra (Fig. S10b), which further verifies the chemical stability of the composite. All these results suggest the remarkable reusability of the composite PCM, thus satisfying the performance requirement for practical applications in the field of solar thermal energy storage.

In addition, the prepared composite (SMG20P) in this work has been compared with the related works in the literature, and the results are recapitulated in Table 2. As can be seen, among all the listed PCM composites, SMG20P showed outstanding thermal performance referring to both its enthalpy efficiency (φ) and photothermal storage efficiency (η) considering the low filler content (φ_f). This proves that GNP/rGO foam as a filler is a good candidate to prepare composite PCMs with excellent thermal properties.

Supplementary video related to this article can be found at https://doi.org/10.1016/j.mtener.2022.101077

4. Conclusions

By introducing active amino groups onto the MF structure, hybrid GNP/rGO foams are facilely prepared through dip-coating followed by air-drying at moderate temperature. The constructed foam shows high hydrophobicity and porosity to efficiently absorb and confine the molten PW. Consequently, the as-prepared PCMs contain high loading of PW (nearly 97 wt%), and thus large latent heat of around 182 J g^{-1} is achieved. The composite PCM samples exhibit an outstanding photothermal energy transition efficiency of up to 92.2%, due to the presence of the photon captor and thermally conductive GNP/rGO layer. Furthermore, the thermal conductivity of the modified MF composite (SMG20P) increases by 87% compared with the composite supported by the pure MF structure, and this improvement was clearly observed using the infrared

camera. Meanwhile, the stiffened foam structure successfully contributed to the shape-stabilization of the composite and also hampered the leakage of the molten PW. Finally, the phase change enthalpy of SMG20P remains unchanged even after 1000 heating and cooling cycles, demonstrating remarkable chemical and thermal stability. All these superior comprehensive properties prove the great potential of the as-prepared PCM composites in the solar-thermal energy storage systems.

CRediT authorship contribution statement

Amir Reza Akhiani: Conceptualization, Methodology, Validation, Formal analysis, Investigation, Data curation, Writing-original draft. Hendrik Simon Cornelis Metselaar: Resources, Review & editing, Supervision, Project administration, Funding acquisition. Bee Chin Ang: Resources, Review & editing, Supervision. Mehdi Mehrali: Validation, Data Curation, Writing-Review & Editing., Mohammad Mehrali: Methodology, Validation, Data Curation, Review & editing, Supervision.

Declaration of competing interest

The authors declare that they have no known competing financial interests or personal relationships that could have appeared to influence the work reported in this paper.

Acknowledgments

The authors were grateful for the research funding for this work from Fundamental Research Grant Scheme (FRGS), Ministry of Higher Education (MOHE), Malaysia (grant no. FP048-2019A). The authors would like to thank Fabia Beckstein from NETZSCH Gerätebau GmbH's Applications Laboratory in Selb, Germany, for her assistance with thermal conductivity measurement and analysis.

Appendix A. Supplementary data

Supplementary data to this article can be found online at https://doi.org/10.1016/j.mtener.2022.101077.

References

[1] B. Koçak, A.I. Fernandez, H. Paksoy, Review on sensible thermal energy storage for industrial solar applications and sustainability aspects, Sol. Energy 209 (2020) 135–169.
[2] A.J. Carrillo, J. González-Aguilar, M. Romero, J.M. Coronado, Solar energy on demand: a review on high temperature thermochemical heat storage systems and materials, Chem. Rev. 119 (7) (2019) 4777–4816.
[3] A. Palacios, C. Barreneche, M.E. Navarro, Y. Ding, Thermal energy storage technologies for concentrated solar power – a review from a materials perspective, Renew. Energy 156 (2020) 1244–1265.
[4] Q. Xu, X. Liu, Q. Luo, Y. Song, H. Wang, M. Chen, Y. Xuan, Y. Li, Y. Ding, Bifunctional biomorphic SiC ceramics embedded molten salts for ultrafast thermal and solar energy storage, Mater. Today Energy 21 (2021), 100764.
[5] H. Zhang, J. Baeyens, G. Cáceres, J. Degrève, Y. Lv, Thermal energy storage: recent developments and practical aspects, Prog. Energy Combust. Sci. 53 (2016) 1–40.
[6] B. Eanest Jebasingh, A. Valan Arasu, A detailed review on heat transfer rate, supercooling, thermal stability and reliability of nanoparticle dispersed organic phase change material for low-temperature applications, Mater. Today Energy 16 (2020), 100408.
[7] Z. Li, E. Gariboldi, Review on the temperature-dependent thermophysical properties of liquid paraffins and composite phase change materials with metallic porous structures, Mater. Today Energy 20 (2021), 100642.
[8] L. Chen, R. Zou, W. Xia, Z. Liu, Y. Shang, J. Zhu, Y. Wang, J. Lin, D. Xia, A. Cao, Electro- and photodriven phase change composites based on wax-infiltrated carbon nanotube sponges, ACS Nano 6 (12) (2012) 10884–10892.
[9] M. Mehrali, S.T. Latibari, M. Mehrali, T.M. Indra Mahlia, H.S. Cornelis Metselaar, M.S. Naghavi, E. Sadeghinezhad, A.R. Akhiani, Preparation and characterization of palmitic acid/graphene nanoplatelets composite with remarkable thermal conductivity as a novel shape-stabilized phase change material, Appl. Therm. Eng. 61 (2) (2013) 633–640.
[10] A.R. Akhiani, M. Mehrali, S. Tahan Latibari, M. Mehrali, T.M.I. Mahlia, E. Sadeghinezhad, H.S.C. Metselaar, One-step preparation of form-stable phase change material through self-assembly of fatty acid and graphene, J. Phys. Chem. C 119 (40) (2015) 22787–22796.
[11] Z. Yang, L. Zhou, W. Luo, J. Wan, J. Dai, X. Han, K. Fu, D. Henderson, B. Yang, L. Hu, Thermally conductive, dielectric PCM–boron nitride nanosheet composites for efficient electronic system thermal management, Nanoscale 8 (46) (2016) 19326–19333.
[12] W. Han, C. Ge, R. Zhang, Z. Ma, L. Wang, X. Zhang, Boron nitride foam as a polymer alternative in packaging phase change materials: synthesis, thermal properties and shape stability, Appl. Energy 238 (2019) 942–951.
[13] F. Li, H. Zhen, L. Li, Y. Li, Q. Wang, X. Cheng, A template-method synthesis of mesoporous-MgO/expanded graphite for enhancing thermal properties of methyl palmitate-lauric acid phase change materials, Mater. Today Energy (2022), 100999.
[14] H.-y. Wu, R.-t. Chen, Y.-w. Shao, X.-d. Qi, J.-h. Yang, Y. Wang, Novel flexible phase change materials with mussel-inspired modification of melamine foam for simultaneous light-actuated shape memory and light-to-thermal energy storage capability, ACS Sustain. Chem. Eng. 7 (15) (2019) 13532–13542.
[15] F. Xue, X.-z. Jin, W.-y. Wang, X.-d. Qi, J.-h. Yang, Y. Wang, Melamine foam and cellulose nanofiber co-mediated assembly of graphene nanoplatelets to construct three-dimensional networks towards advanced phase change materials, Nanoscale 12 (6) (2020) 4005–4017.
[16] F. Xue, Y. Lu, X.-d. Qi, J.-h. Yang, Y. Wang, Melamine foam-templated graphene nanoplatelet framework toward phase change materials with multiple energy conversion abilities, Chem. Eng. J. 365 (2019) 20–29.
[17] H. Liao, W. Chen, Y. Liu, Q. Wang, A phase change material encapsulated in a mechanically strong graphene aerogel with high thermal conductivity and excellent shape stability, Compos. Sci. Technol. 189 (2020), 108010.
[18] M. Peng, G. Chen, G. Zeng, A. Chen, K. He, Z. Huang, L. Hu, J. Shi, H. Li, L. Yuan, T. Huang, Superhydrophobic kaolinite modified graphene oxide-melamine sponge with excellent properties for oil-water separation, Appl. Clay Sci. 163 (2018) 63–71.
[19] Z. Lei, G. Zhang, Y. Deng, C. Wang, Surface modification of melamine sponges for pH-responsive oil absorption and desorption, Appl. Surf. Sci. 416 (2017) 798–804.
[20] V.H. Pham, J.H. Dickerson, Superhydrophobic silanized melamine sponges as high efficiency oil absorbent materials, ACS Appl. Mater. Interfaces 6 (16) (2014) 14181–14188.
[21] C. Zhang, R. Huang, Y. Wang, Z. Wu, H. Zhang, Y. Li, W. Wang, C. Huang, L. Li, Self-assembled boron nitride nanotube reinforced graphene oxide aerogels for dielectric nanocomposites with high thermal management capability, ACS Appl. Mater. Interfaces 12 (1) (2020) 1436–1443.
[22] S. Mypati, A. Sellathurai, M. Kontopoulou, A. Docoslis, D.P.J. Barz, High concentration graphene nanoplatelet dispersions in water stabilized by graphene oxide, Carbon 174 (2021) 581–593.
[23] O.C. Compton, D.A. Dikin, K.W. Putz, L.C. Brinson, S.T. Nguyen, Electrically conductive "alkylated" graphene paper via chemical reduction of amine-functionalized graphene oxide paper, Adv. Mater. 22 (8) (2010) 892–896.
[24] J. Nam, S. Yang, B.Y. Yun, S. Kim, Evaluation of thermal/morphological performance of SSPCM based nanoclay: influence of the interlayer microstructure of hydrophilic and hydrophobic, Sol. Energy Mater. Sol. Cells 235 (2022), 111479.
[25] H. Zhu, D. Chen, W. An, N. Li, Q. Xu, H. Li, J. He, J. Lu, A robust and cost-effective superhydrophobic graphene foam for efficient oil and organic solvent recovery, Small 11 (39) (2015) 5222–5229.
[26] C. Liu, S. Qiu, P. Du, H. Zhao, L. Wang, An ionic liquid–graphene oxide hybrid nanomaterial: synthesis and anticorrosive applications, Nanoscale 10 (17) (2018) 8115–8124.
[27] Y. Ding, W. Xu, Y. Yu, H. Hou, Z. Zhu, One-step preparation of highly hydrophobic and oleophilic melamine sponges via metal-ion-induced wettability transition, ACS Appl. Mater. Interfaces 10 (7) (2018) 6652–6660.
[28] N.H.T. Tran, J. Kim, T.B. Phan, S. Khym, H. Ju, Label-free optical biochemical sensors via liquid-cladding-induced modulation of waveguide modes, ACS Appl. Mater. Interfaces 9 (37) (2017) 31478–31487.
[29] I. Ismail, J. Wei, X. Sun, W. Zha, M. Khalil, L. Zhang, R. Huang, Z. Chen, Y. Shen, F. Li, Q. Luo, C.-Q. Ma, Simultaneous improvement of the long-term and thermal stability of the perovskite solar cells using 2,3,4,5,6-pentafluorobenzoyl chloride (PFBC)-Capped ZnO nanoparticles buffer layer, Sol. RRL 4 (10) (2020), 2000289.
[30] D. Wu, B. Ni, Y. Liu, S. Chen, H. Zhang, Preparation and characterization of side-chain liquid crystal polymer/paraffin composites as form-stable phase change materials, J. Mater. Chem. 3 (18) (2015) 9645–9657.
[31] Y. Li, Y.A. Samad, K. Polychronopoulou, S.M. Alhassan, K. Liao, From biomass to high performance solar–thermal and electric–thermal energy conversion and storage materials, J. Mater. Chem. 2 (21) (2014) 7759–7765.
[32] Y. Wang, H. Wang, F. Liu, X. Wu, J. Xu, H. Cui, Y. Wu, R. Xue, C. Tian, B. Zheng, W. Yao, Flexible printed circuit board based on graphene/polyimide composites with excellent thermal conductivity and sandwich structure, Compos. Appl. Sci. Manuf. 138 (2020), 106075.
[33] R.A. Manzhos, S.A. Baskakov, E.N. Kabachkov, V.I. Korepanov, N.N. Dremova, Y.V. Baskakova, A.G. Krivenko, Y.M. Shulga, G.L. Gutsev, Reduced graphene

oxide aerogel inside melamine sponge as an electrocatalyst for the oxygen reduction reaction, Materials 14 (2) (2021) 322.
[34] G. Zhu, C. Xi, Y. Liu, J. Zhu, X. Shen, CN foam loaded with few-layer graphene nanosheets for high-performance supercapacitor electrodes, J. Mater. Chem. 3 (14) (2015) 7591–7599.
[35] Y. Zhang, Q. Zhang, R. Zhang, S. Liu, Y. Zhou, A superhydrophobic and elastic melamine sponge for oil/water separation, New J. Chem. 43 (16) (2019) 6343–6349.
[36] T. Zhou, S. Huang, D. Niu, L. Su, G. Zhen, Y. Zhao, Efficient separation of water-soluble humic acid using (3-aminopropyl)triethoxysilane (APTES) for carbon resource recovery from wastewater, ACS Sustain. Chem. Eng. 6 (5) (2018) 5981–5989.
[37] N. Mostofi Sarkari, Ö. Doğan, E. Bat, M. Mohseni, M. Ebrahimi, Assessing effects of (3-aminopropyl)trimethoxysilane self-assembled layers on surface characteristics of organosilane-grafted moisture-crosslinked polyethylene substrate: a comparative study between chemical vapor deposition and plasma-facilitated in situ grafting methods, Appl. Surf. Sci. 497 (2019), 143751.
[38] K.C. Wasalathilake, D.G.D. Galpaya, G.A. Ayoko, C. Yan, Understanding the structure-property relationships in hydrothermally reduced graphene oxide hydrogels, Carbon 137 (2018) 282–290.
[39] A. Deryło-Marczewska, J. Goworek, S. Pikus, E. Kobylas, W. Zgrajka, Characterization of Melamine–Formaldehyde resins by XPS, SAXS, and sorption techniques, Langmuir 18 (20) (2002) 7538–7543.
[40] Y. Wu, Q. Fang, X. Yi, G. Liu, R.-W. Li, Recovery of gold from hydrometallurgical leaching solution of electronic waste via spontaneous reduction by polyaniline, Prog. Nat. Sci. 27 (4) (2017) 514–519.
[41] S. Ravi, S. Zhang, Y.-R. Lee, K.-K. Kang, J.-M. Kim, J.-W. Ahn, W.-S. Ahn, EDTA-functionalized KCC-1 and KIT-6 mesoporous silicas for Nd3+ ion recovery from aqueous solutions, J. Ind. Eng. Chem. 67 (2018) 210–218.
[42] M. Singh, N. Kaur, G. Drera, A. Casotto, L. Sangaletti, E. Comini, SAM functionalized ZnO nanowires for selective acetone detection: optimized surface specific interaction using APTMS and GLYMO monolayers, Adv. Funct. Mater. 30 (38) (2020), 2003217.
[43] S. Nsanzamahoro, F.P. Mutuyimana, Y. Han, S. Ma, M. Na, J. Liu, Y. Ma, C. Ren, H. Chen, X. Chen, Highly selective and sensitive detection of catechol by one step synthesized highly fluorescent and water-soluble silicon nanoparticles, Sens. Actuator B-Chem. 281 (2019) 849–856.
[44] P.M. Dietrich, C. Streeck, S. Glamsch, C. Ehlert, A. Lippitz, A. Nutsch, N. Kulak, B. Beckhoff, W.E.S. Unger, Quantification of silane molecules on oxidized silicon: are there options for a traceable and absolute determination? Anal. Chem. 87 (19) (2015) 10117–10124.
[45] A. Stolz, S. Le Floch, L. Reinert, S.M.M. Ramos, J. Tuaillon-Combes, Y. Soneda, P. Chaudet, D. Baillis, N. Blanchard, L. Duclaux, A. San-Miguel, Melamine-derived carbon sponges for oil-water separation, Carbon 107 (2016) 198–208.
[46] P. Visuvamithiran, M. Palanichamy, K. Shanthi, V. Murugesan, Selective epoxidation of olefins over Co(II)-Schiff base immobilised on KIT-6, Appl. Catal. A-Gen. 462–463 (2013) 31–38.
[47] M. Mehrali, S.T. Latibari, M. Mehrali, H.S.C. Metselaar, M. Silakhori, Shape-stabilized phase change materials with high thermal conductivity based on paraffin/graphene oxide composite, Energy Convers. Manag. 67 (2013) 275–282.
[48] Y. Luo, Y. Xie, H. Jiang, Y. Chen, L. Zhang, X. Sheng, D. Xie, H. Wu, Y. Mei, Flame-retardant and form-stable phase change composites based on MXene with high thermostability and thermal conductivity for thermal energy storage, Chem. Eng. J. 420 (2021), 130466.
[49] J. Wang, X. Jia, D.G. Atinafu, M. Wang, G. Wang, Y. Lu, Synthesis of “graphene-like” mesoporous carbons for shape-stabilized phase change materials with high loading capacity and improved latent heat, J. Mater. Chem. 5 (46) (2017) 24321–24328.
[50] M. Mehrali, J.E. ten Elshof, M. Shahi, A. Mahmoudi, Simultaneous solar-thermal energy harvesting and storage via shape stabilized salt hydrate phase change material, Chem. Eng. J. 405 (2021), 126624.
[51] Y. Zhang, J. Wang, J. Qiu, X. Jin, M.M. Umair, R. Lu, S. Zhang, B. Tang, Ag-graphene/PEG composite phase change materials for enhancing solar-thermal energy conversion and storage capacity, Appl. Energy 237 (2019) 83–90.
[52] J. Yang, G.-Q. Qi, Y. Liu, R.-Y. Bao, Z.-Y. Liu, W. Yang, B.-H. Xie, M.-B. Yang, Hybrid graphene aerogels/phase change material composites: thermal conductivity, shape-stabilization and light-to-thermal energy storage, Carbon 100 (2016) 693–702.
[53] G. Qi, J. Yang, R. Bao, D. Xia, M. Cao, W. Yang, M. Yang, D. Wei, Hierarchical graphene foam-based phase change materials with enhanced thermal conductivity and shape stability for efficient solar-to-thermal energy conversion and storage, Nano Res. 10 (3) (2017) 802–813.
[54] L. Zhang, R. Li, B. Tang, P. Wang, Solar-thermal conversion and thermal energy storage of graphene foam-based composites, Nanoscale 8 (30) (2016) 14600–14607.
[55] G. Li, X. Zhang, J. Wang, J. Fang, From anisotropic graphene aerogels to electron- and photo-driven phase change composites, J. Mater. Chem. 4 (43) (2016) 17042–17049.
[56] J. Yang, G.-Q. Qi, R.-Y. Bao, K. Yi, M. Li, L. Peng, Z. Cai, M.-B. Yang, D. Wei, W. Yang, Hybridizing graphene aerogel into three-dimensional graphene foam for high-performance composite phase change materials, Energy Storage Mater. 13 (2018) 88–95.
[57] M. Su, G. Han, J. Gao, Y. Feng, C. He, J. Ma, C. Liu, C. Shen, Carbon welding on graphene skeleton for phase change composites with high thermal conductivity for solar-to-heat conversion, Chem. Eng. J. 427 (2022), 131665.
[58] S. Xi, M. Wang, L. Wang, H. Xie, W. Yu, 3D reduced graphene oxide aerogel supported TiO2-x for shape-stable phase change composites with high photothermal efficiency and thermal conductivity, Sol. Energy Mater. Sol. Cells 226 (2021), 111068.